NUMERICAL METHODS FOR CAVITATING FLOW

Byeong Rog SHIN [1]

In this paper, some numerical methods recently developed for gas-liquid two-phase flows are reviewed. And then, a preconditioning method to solve cavitating flow by the author is introduced. This method employs a finite-difference Runge-Kutta method combined with MUSCL TVD scheme, and a homogeneous equilibrium cavitation model. So that it permits to treat simply the whole gas-liquid two-phase flow field including wave propagation, large density changes and incompressible flow characteristic at low Mach number. Finally, numerical results such as detailed observations of the unsteady cavity flows, a sheet cavitation break-off phenomena and some data related to performance characteristics of hydrofoils are shown.

1. Introduction

Cavitation is a phase change phenomenon occurred in some domain below vapor pressure according to the decrease of local pressure when fluid devices such as hydrofoils, rocket engine turbopumps, marine propellers and water-going vessels move with a high-speed in working fluid of liquid state. When cavitation occurs unexpectedly accompanying the attachment and collapsing of cavitation bubbles near solid surfaces, it causes the noise, vibration and damage as well as changes the performance characteristics in hydraulic machine systems [1]. As the results, it has an unfavorable effect on the performance and eventually brings the low efficiency. In the sense of reducing these, therefore, technology of accurate prediction and estimation of cavitation are very important in development of high-speed fluid devices.

To clarify and understand the behavior of cavity flow, some efforts to propose cavity flow model and analytical method for numerical simulations have been made. For instance, they are interface-tracking methodologies [2,3] and gas-liquid two-phase flow approaches with thermodynamic effects [4,5], concept of the homogeneous equilibrium [6,7], unsteady flow effects and treatment as a compressible medium [8-10]. Up to date, however, because originally the cavity flows have strong unsteady flow phenomena including phase changes, fluid transients, vortex shedding and turbulence, the numerical method to solve these flows is not established yet. In general, they have had little comprehensive applications to the transient flow range from subcavitation state to supercavitation state. Lately, the present author and co-workers have proposed a mathematical cavity flow model [11,12] based on a homogeneous equilibrium model taking account of the compressibility of the gas-liquid two-phase media. With this model and TVD-MacCormack scheme [13] or a high-order MUSCL TVD [14] solution method, the mechanism of developing cavitation has been investigated through the application to a couple of cavitating flows around a hydrofoil [15-18].

The purpose of this paper is to verify an applicability of the above mathematical model to the wide range of cavity flow through cascade, and to extend a high-order MUSCL TVD solution method to a preconditioning method to treat incompressible flow characteristic at low Mach number. As the numerical examples, an unsteady cavity flows through a two-dimensional (2-D) decelerating cascade are simulated. And then, detailed unsteady cavity flow behavior including the growing and shedding of the cavity for the above flow fields are investigated. Pressure distributions obtained by the present preconditioned and non-preconditioned solution method are compared with experimental data. Some data to predict performance characteristics of hydrofoils in cascades for cavitating flow is provided.

2. Mathematical Model of Cavitating Flow

Gas-liquid two-phase flow of cavity flow is possible to model into an apparent single-phase flow by using concept of the homogeneous equilibrium model in which thermodynamic equilibrium is assumed and velocity slip between both phases is neglected. When we consider a local volumetric element in gas-liquid two-phase media, where numerous particles of infinitesimal bubbles or droplets are assumed to distribute homogeneously, the two-phase media may model mesoscopically by the infinite set of these elements with each different void fraction. That is, cavitation bubbles can be expressed by arranging homogenized elements according to their shapes.

[1] Associate Professor, Institute of Fluid Science, Tohoku University, 2-1-1 Katahira, Aoba-ku, Sendai 980-8577, Japan. E-mail:shin@ifs.tohoku.ac.jp, http://cfs.ifs.tohoku.ac.jp/. Life Member KSCFE.

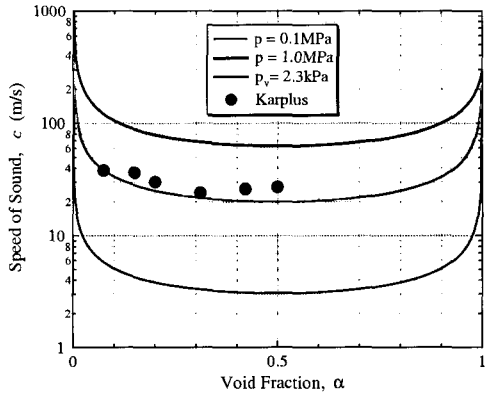

Fig.1 Sound speed and void fraction at 20°C

Under the above model concept, the pressure for gas-liquid two-phase media is determined by using a combination of two equations of state for gas phase and liquid phase, that is written as follows:

$$\rho = \frac{p(p+p_c)}{K(1-Y)p(T+T_c)+RY(p+p_c)T} \tag{1}$$

where, ρ, p, Y, and T are the mixture density, pressure, quality (dryness) and the temperature, respectively. R is the gas constant and K, p_c and T_c represent the liquid constant, pressure constant and the temperature constant for water, respectively. This equation is derived from the local equilibrium assumption, and corresponds to the following equations of state for pure liquid (Y=0) by Tammann [19] and ideal gas (Y=1), respectively.

$$\begin{aligned} &p+p_c = \rho_\ell K(T+T_c); \quad \text{for Y=0,} \\ &p = \rho_g RT; \qquad\qquad\quad \text{for Y=1} \end{aligned} \tag{2}$$

where, subscripts ℓ and g mean liquid phase and gas phase. Therefore, the apparent compressibility is considered, and the sound speed c becomes

$$c^2 = \rho C_p(\frac{\partial \rho}{\partial T} + \rho C_p \frac{\partial \rho}{\partial p})^{-1} = C_p(p+p_c)^2 p/\rho c_1 \tag{3}$$

where, $c_1 = (p+p_c)^2(C_p - YR) - C_p(1-Y)\rho K(T+T_c)p_c - (1-Y)Kp(p+p_c)$. C_p is the specific heat capacity at constant pressure of $C_p = YC_{pg} + (1-Y)C_{p\ell}$. And, the relation between the local void fraction α and the quality Y is given as $\rho(1-Y) = (1-\alpha)\rho_\ell$ and $\rho Y = \alpha\rho_g$, where

$$\alpha = \frac{RY(p+p_c)T}{K(1-Y)p(T+T_c)+RY(p+p_c)T} \tag{4}$$

Figure 1 shows a sound speed-void fraction relationship at an atmospheric temperature of T = 293K. The constants p_c, K and T_c for water in above equations were estimated as 1944.61MPa, 472.27J/KgK and 3837K, respectively. Speed of sound predicted by Eq.(3) is well compared with Karplus' [20] experimental data.

3. Governing Equations

The hydraulic flow including cavitations can be characterized as fully 3-D non-linear, viscous flow with laminar and turbulent regions. Also this flow with hydraulic transients and hydroacoustics presents the compressible flow characteristic at low Mach number. For such flow, compressible flow model with preconditioning method [21-24] is advantageous. Preconditioning is a way to extend the functionality of existing codes for fully compressible flows to almost incompressible flows.

Based on above modeling concept and neglecting the surface tension, the 2-D preconditioned governing equations for the mixture mass, momentum, energy and the gas-phase mass can be written in the curvilinear coordinates as follows:

$$\Gamma^{-1}\frac{\partial \boldsymbol{W}}{\partial t} + \frac{\partial(\boldsymbol{E}-\boldsymbol{E}_v)}{\partial \xi} + \frac{\partial(\boldsymbol{F}-\boldsymbol{F}_v)}{\partial \eta} = 0 \tag{5}$$

where $\boldsymbol{W}$ is the unknown variable vector, $\boldsymbol{E}$ and $\boldsymbol{F}$ are the flux vectors and $\boldsymbol{E}_v$ and $\boldsymbol{F}_v$ are the viscous terms presented by the stress tensor τ of the compressible Navier-Stokes flow.

$$\boldsymbol{W} = \begin{pmatrix} p \\ u \\ v \\ T \\ Y \end{pmatrix}, \quad \boldsymbol{E} = J \begin{pmatrix} \rho U \\ \rho u U + \xi_x p \\ \rho v U + \xi_y p \\ \rho U H \\ \rho U Y \end{pmatrix}, \quad \boldsymbol{F} = J \begin{pmatrix} \rho V \\ \rho u V + \eta_x p \\ \rho v V + \eta_y p \\ \rho V H \\ \rho V Y \end{pmatrix},$$

$$\boldsymbol{E}_v = J \begin{pmatrix} 0 \\ \xi_x \tau_{xx} + \xi_y \tau_{xy} \\ \xi_x \tau_{yx} + \xi_y \tau_{yy} \\ \xi_x T_{11} + \xi_y T_{22} \\ 0 \end{pmatrix}, \quad \boldsymbol{F}_v = J \begin{pmatrix} 0 \\ \eta_x \tau_{xx} + \eta_y \tau_{xy} \\ \eta_x \tau_{yx} + \eta_y \tau_{yy} \\ \eta_x T_{11} + \eta_y T_{22} \\ 0 \end{pmatrix}$$

where, $T_{11} = u\tau_{xx} + v\tau_{xy} + \kappa \partial T/\partial x$, $T_{22} = u\tau_{yx} + v\tau_{yy} + \kappa \partial T/\partial y$ and κ is the coefficient of thermal conductivity.

In this study, the preconditioning matrix Γ^{-1} is formed by the addition of the vector $\theta[1, u, v, H, Y]^T$ to the first column of the Jacobian matrix $\partial \boldsymbol{Q}/\partial \boldsymbol{W}$, where $\boldsymbol{Q}(= J[\rho, \rho u, \rho v, e, \rho Y]^T)$ is the conservative unknown variables. Parameter θ is chosen by Choi & Merkle [22] and Weiss & Smith [25],

$$\theta = \frac{1}{a^2} - \frac{1}{c^2},$$
$$a^2 = \min[c^2, \max(|\boldsymbol{u}|^2, \beta |U_0|^2)] \tag{6}$$

where, $|U_0|$ is a fixed reference velocity such as an average incoming freestream velocity, β is a constant. H in Eq.(5) is enthalpy defined by total energy $e = \rho H - p$.

The Jacobian J of the transformation between Cartesian coordinates x_i and curvilinear coordinates ξ_i is defined by $J = x_\xi y_\eta - x_\eta y_\xi$. u_i is the physical velocity and U_i is the contravariant velocity. The mixture density ρ and the mixture viscosity μ can be expressed by $\rho = (1-\alpha)\rho_\ell + \alpha \rho_g$, and $\mu = (1-\alpha)(1+2.5\alpha)\mu_\ell + \alpha \mu_g$ [26].

4. Numerical Methods

In this paper, the governing equations (5) are numerically integrated by using the finite-difference third-order Runge-Kutta explicit method. And then the Roe's flux difference splitting (FDS) method [27] with the MUSCL TVD scheme [14] is applied to enhance the numerical stability, especially for the existence of steep gradient in density as well as pressure near the gas-liquid interface. Therefore, the derivative of the flux vector, for instance, $\boldsymbol{E}$ with respect to ξ at point i can be written with the numerical flux as $(\partial \boldsymbol{E}/\partial \xi) = (\boldsymbol{E}_{i+1/2} - \boldsymbol{E}_{i-1/2})/\Delta\xi$ and then, the approximate Riemann solver based on the Roe's FDS is applied. Hence, the numerical flux $\boldsymbol{E}_{i+1/2}$ is written as,

$$\boldsymbol{E}_{i+1/2} = (1/2)\{\boldsymbol{E}(\boldsymbol{Q}^L_{i+1/2}) + \boldsymbol{E}(\boldsymbol{Q}^R_{i+1/2}) - \Gamma^{-1}_{i+1/2}(\boldsymbol{L_p}^{-1}|\Lambda|\boldsymbol{L_p})_{i+1/2}(\boldsymbol{W}^R_{i+1/2} - \boldsymbol{W}^L_{i+1/2})\} \tag{7}$$

where, $\Lambda = (U, \tilde{U} + \tilde{c}, U, \tilde{U} - \tilde{c}, U)^D$ is the diagonal matrix of eigenvalues and $\boldsymbol{L_p}$ and $\boldsymbol{L_p}^{-1}$ are the left eigenvectors of $\Gamma \partial \boldsymbol{E}/\partial \boldsymbol{W}$. $\tilde{U} \pm \tilde{c} = U - (EV)^{\mp}/2$, and

$$\boldsymbol{L_p} = \begin{pmatrix} 1 & 0 & 0 & -\rho C_p & 0 \\ 1 & \xi_x \ell^- & \xi_y \ell^- & 0 & 0 \\ 0 & \xi_y & -\xi_x & 0 & 0 \\ 1 & \xi_x \ell^+ & \xi_y \ell^+ & 0 & 0 \\ 0 & -\xi_y & \xi_x & 0 & 1 \end{pmatrix}, \qquad \ell^{\pm} = \frac{-2}{(EV)^{\pm}} \rho c^2 A,$$

$$(EV)^{\pm} = B \pm \sqrt{B^2 + 4Ac^2 g_{11}}, \qquad A = \frac{\rho_T + \rho C_p \rho_p}{\rho_T + \rho C_p(\theta + \rho_p)}, \qquad B = \frac{U \rho C_p \theta}{\rho_T + \rho C_p(\theta + \rho_p)}$$

where, $\rho_\alpha = \partial \rho/\partial \alpha$, $g_{11} = \xi_x^2 + \xi_y^2$ and the eigenvectors are estimated introducing the Roe's averaging. $\boldsymbol{W}^{L,R}_{i+1/2}$ is obtained by applying the third-order MUSCL TVD scheme as

$$\boldsymbol{W}^L_{i+1/2} = \boldsymbol{W}_i + (1/4)\{(1-\kappa)D^+ \boldsymbol{W}_{i-1/2} + (1+\kappa)D^- \boldsymbol{W}_{i+1/2}\}$$
$$\boldsymbol{W}^R_{i+1/2} = \boldsymbol{W}_{i+1} - (1/4)\{(1-\kappa)D^- \boldsymbol{W}_{i+3/2} + (1+\kappa)D^+ \boldsymbol{W}_{i+1/2}\} \tag{8}$$

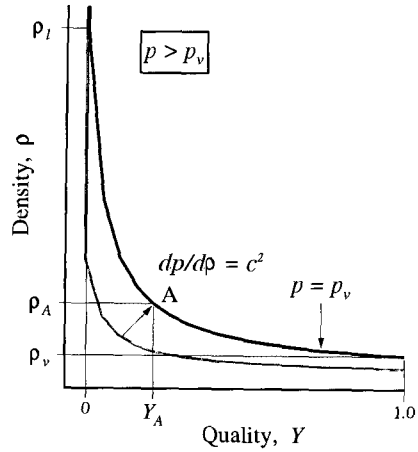

Fig.2 State law of the liquid-vapor mixture

Here, the flux-limited values of $D\boldsymbol{W}$ and the minmod function are determined by

$$
\begin{aligned}
&D^{+}\boldsymbol{W}_{i-1/2} = \text{minmod}(\delta\boldsymbol{W}_{i-1/2}, b\delta\boldsymbol{W}_{i+1/2}),\\
&D^{-}\boldsymbol{W}_{i+1/2} = minmod(\delta\boldsymbol{W}_{i+1/2}, b\delta\boldsymbol{W}_{i-1/2}),\\
&\delta\boldsymbol{W}_{i+1/2} = \boldsymbol{W}_{i+1} - \boldsymbol{W}_{i},\\
&minmod(x,y) = sign(x)max|0, \min\{|x|, ysign(x)\}|
\end{aligned}
\tag{9}
$$

And, the linear combination parameter κ is determined by the range of $-1 \le \kappa \le 1$, and it has an effect on the accuracy, that is Eq.(8) has a third-order accuracy at $\kappa = 1/3$. The slope of the flux in the minmod function is controlled by the limiter b. The range of b, $1 \le b \le (3-\kappa)/(1-\kappa)$, is determined by the condition of TVD stable. In this computation, b of 4 and κ of $1/3$ is employed.

In the numerical integration of governing equations (5), the third-order TVD Runge-Kutta explicit method written followings is used.

$$\boldsymbol{W}^{(1)} = \boldsymbol{W}^{n} - \Delta t\Gamma\boldsymbol{L}(\boldsymbol{Q}^{n}) \tag{10}$$

$$\boldsymbol{W}^{(2)} = \frac{3}{4}\boldsymbol{W}^{n} + \frac{1}{4}\{\boldsymbol{W}^{(1)} - \Delta t\Gamma\boldsymbol{L}(\boldsymbol{Q}^{(1)})\} \tag{11}$$

$$\boldsymbol{W}^{n+1} = \frac{1}{3}\boldsymbol{W}^{n} + \frac{2}{3}\{\boldsymbol{W}^{(2)} - \Delta t\Gamma\boldsymbol{L}(\boldsymbol{Q}^{(2)})\} \tag{12}$$

where,

$$\boldsymbol{L}(\boldsymbol{Q}) = \frac{\partial(\boldsymbol{E}-\boldsymbol{E}_v)}{\partial\xi} + \frac{\partial(\boldsymbol{F}-\boldsymbol{F}_v)}{\partial\eta}$$

Phase change occurs spontaneously depending on the equation of state and the pressure fields expressed by the mixture density in Eqs.(1) and (2). In the region of local pressures below the vapor pressure, however, the phase change can be expressed by the way that the vapor pressure (p_v) substitutes the local pressures. And then, density is determined by the isentropic assumption as illustrated in Fig.2. To consider the vapor pressure at any temperatures below the critical temperature, a new industrial standard called as the IAPWS thermodynamic properties of water and steam is used.

5. Numerical Results

The present computational methods have been validated for the noncavity flow around a hydrofoil in a decelerating cascade, in which the blade profile is a Clark Y 11.7% hydrofoil. The pitch-chord ratio is 0.9 and the stagger angle is 30deg. The Reynolds number Re based on the inlet mean velocity is about 2×10^5. An ordinary compressible flow boundary condition is imposed.

Figure 3 shows time-averaged pressure distributions at two different angles of attack (α_i) measured with inlet velocities. As a whole, the comparison of predictions for noncavity flow with experiments using wind tunnel [28] is favorable. In this noncavity flow computation, two-phase flows without cavitation were approximated by the single-phase. However, the results by non-preconditioned formula are somewhat fluctuated

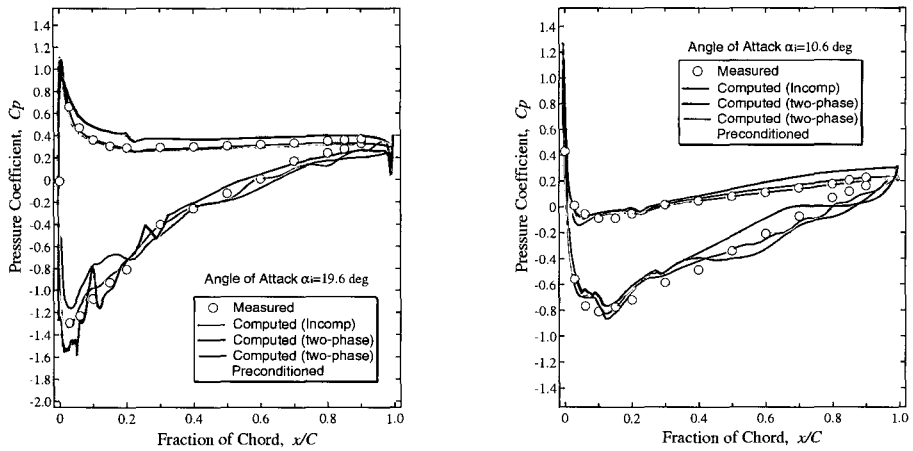

Fig.3 Comparison of pressure distributions

near leading edge on suction surface and over predicted on pressure surfaces even though, to reduce numerical instability, finer grids and farther boundaries than those for preconditioned formula are used. In the computation with non-preconditioning [16], the up- and down-stream boundaries of the computational domain are located at each 5 times chord length C distances from the leading edge and trailing edge of the hydrofoil. A body fitted H-type computational grid having 321×121 grid points is used. On the other hand, in preconditioning, $2C$ and $5C$ of up- and down-stream boundaries and 211×81 grid points are used. As convincing reasons of the fluctuation, stiffness of non-preconditioning method for nearly incompressible flow and insufficient time-averaging are considered. Because very small time step is adopted to reduce the instability, total dimensional time used in time-averaging is relatively short compared with the number of iterations.

The results by preconditioning with β of 50 in Eq.(6) are much closer to those of experiments [28] and computation by an efficient incompressible Navier-Stokes solver [29]. In the preconditioning method, available time increment increased up to about a hundred times of non-preconditioning one for the noncavity flow. The time-averaged results between two and five seconds shown in Fig.4 are still shown a wavy flow pattern in rear part of suction surface due to the time dependent flow separation. Figure 4 shows a time history of lift (C_L) and drag (C_D) coefficients at $\alpha_i = 19.6$deg by the preconditioning shown in Fig.3. As far as we predict with this result, their periods are roughly one second. C_L, C_D values estimated with a mean properties (by subscript m) between one chord of up- and down-stream boundaries are very reasonable compared with experiments [28,30] in Fig.5.

Another comparison to validate the applicability of preconditioning is shown in Fig.6. Two results of time-averaged pressure contours are agreed well with each other. At about 20% chord on suction surface in Fig.6(b), pressure predicted by preconditioning is showing a sort of secondary peak.

Next, using the present preconditioning method, cavitating flows are calculated at two different cavitation numbers. Here, the cavitation number σ is defined by $\sigma = 2(p_0 - p_v)/\rho_0 u_0^2$ using mean values at upstream of

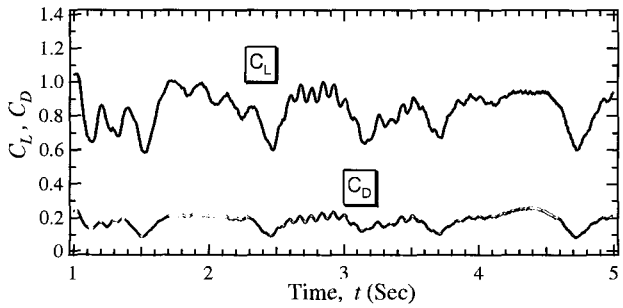

Fig.4 Time history of lift and drag coefficients at $\alpha_i = 19.6°$

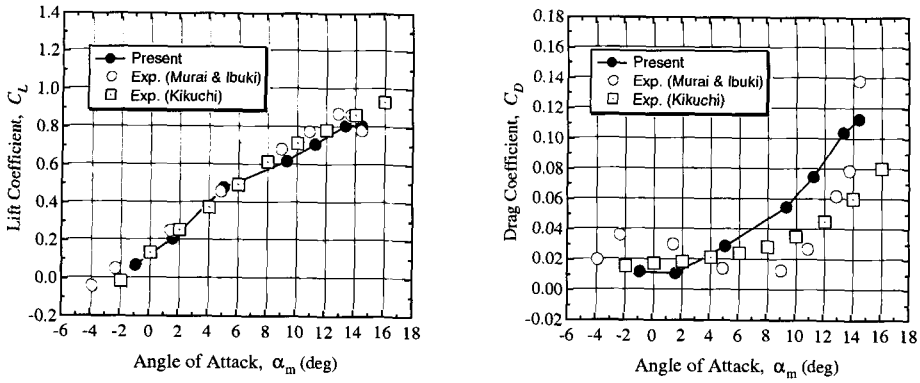

Fig.5 Comparison of lift and drag coefficients

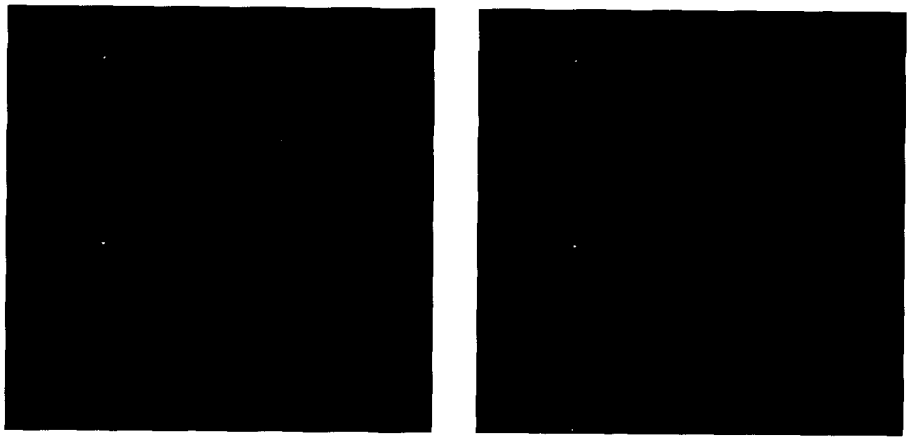

(a) (b)

Fig.6 Time-averaged pressure contours by (a) incompressible flow solver and (b) preconditioning method

the hydrofoil and the vapor pressure p_v. With low cavitation number, relatively low pressure is distributed on blade surfaces as shown in Fig.7(a) and cavitation is more likely occurs. At σ=0.51, a sheet cavitation is formed near leading edge and, it shows $Cp \approx -\sigma$ at 2%~10% chord region of suction surface. At σ=0.41, however, the cavitating flow indicates a supercavitating state. That is, relatively large sheet cavity is formed, so that Cp values on suction side present approximately the value of $-\sigma$. Because of a thermodynamic effect, the Cp on suction surface shows somewhat a curve. To illustrate this effect on the cavitation performance, a demonstrative comparison of the temperature depressions between σ of 0.51 and 0.41 is presented in Fig.7(b). As can be seen, the temperature depressions is very small for water at working temperature of T_0 = 293K, but the local vapor pressure change due to subcooling is expected. For cryogenic fluids with strong dependence of vapor pressure, the thermodynamic effects are important because the dependence can lead to substantially different predictions of cavitation performance. In general it is well known that the cavity is much over-predicted when the thermodynamic effects are neglected. In this cavitation numbers, fluctuations of C_L and C_D were milder than that of noncavitating case in Fig.4 due to the large and nearly stationary separation involving cavitation formed on suction surface [31].

Figures 8 and 9 show a time-averaged pressure, density, void fraction and temperature contours at σ of 0.51 and 0.41, respectively. In these color graphics, the red presents higher values. At a high angle of attack, cavitating flow forms relatively strong shear layer on suction surface, and slightly low temperature is distributed in the region of cavity flow. These results are related to cavitating flow characteristics including

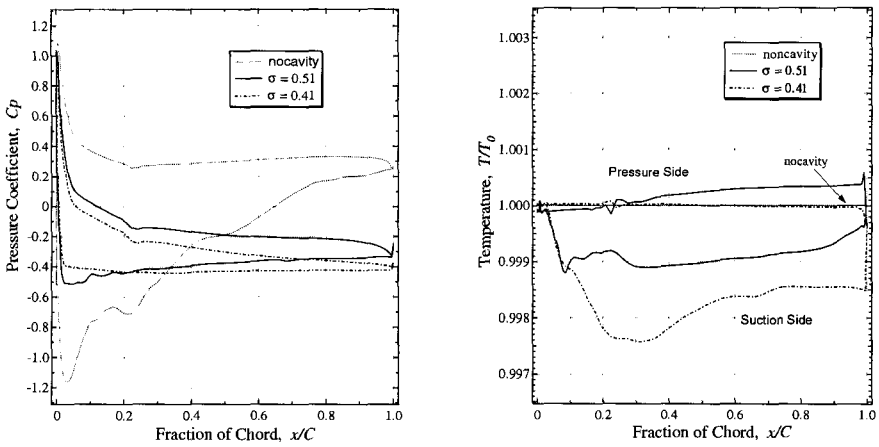

(a) Pressure (b) Temperature

Fig.7 Pressure and temperature distribution at different cavitation number

C_p, C_L and C_D distributions examined so far.

Figure 10 shows time evolutions of instantaneous void fraction around the hydrofoil at σ=0.6, α_i = 10.6deg and moderately high Reynolds number $Re = 7 \times 10^5$. In this case, computation was performed with isothermal condition and without preconditioning as conducted in Ref.[16]. The behavior of this cavitating flow indicates a kind of transient cavitation state. The occurrence and the development of the sheet cavitation are similar to the subcavitating state. However, the fluctuation on the cavity length and thickness becomes much stronger. The internal structure of the cavity on the void fraction is clear. It can be seen that the cavitation occurred near 10% chord on the suction surface is developing and shedding toward downstream with time. After Fig.12(f), a wavy cloud cavitation came off the suction surface and then the sheet cavitation was formed again. A time-averaged void fraction and pressure contours at σ=0.6 and α=10.6deg seen in Fig.10 are shown in Fig.11. The cavity flow pattern indicates aforementioned transient cavitation state. Also, a typical pressure distribution of cascade is shown in this figure, where the region surrounded by inner contour line on suction surface is that representing near vapor pressure.

6. Conclusions

To analyze gas-liquid two-phase flows such as cavitating flows, a numerical method using preconditioning method was proposed. In the proposed method, a finite-difference Runge-Kutta method combined with MUSCL TVD scheme is employed, and a homogeneous equilibrium model of cavitating flow is applied.

Using this method, 2-D cavitating flows through a decelerating cascade were numerically simulated. As the result, it is confirmed that the present preconditioning method gave us good computational performance compared with non-preconditioning one. And it showed a successive application to cavitating cascade flows, and a good prediction of lift and drag coefficients and pressure distributions in comparison with experiments. From investigation of the void fraction and velocity field in the cavity, complex cavity flow behaviors of the cavitation occurrence and its growing and shedding were understood.

References

[1] Brennen, C.E., *Hydrodynamics of Pumps*, Oxford Univ. Press, Oxford (1994)
[2] Chen, Y. and Heister, S.D., ASME J. Fluids Engng, **116** (1994), p.613
[3] Deshpande, M. et al., ASME J. of Fluids Engng **119**, (1997), p.420
[4] Cooper, P., ASME J. of Engng for Power, October (1967), p.577
[5] Singhal, A.K. et al., ASME FEDSM97-3272 (1997)
[6] Merkle, C.L. et al., Proc. 3rd Int. Symp. on Cavitation, Vol.2 (1998), p.307
[7] Chen, Y. and Heister, S.D., Computers & Fluids, **24** (1995), p.799
[8] Reboud, J.L. and Delannoy, Y., Proc. 2nd Int. Symp. on Cavitation (1994), p.39
[9] Janssens, M.E. et al., AIAA paper 97-1936 (1997)
[10] Ventikos, Y. and Tzabiras, G., Computers & Fluids, **29** (2000), p.63
[11] Okuda, K. and Ikohagi, T., Trans JSME B **62** (1996), p.3792

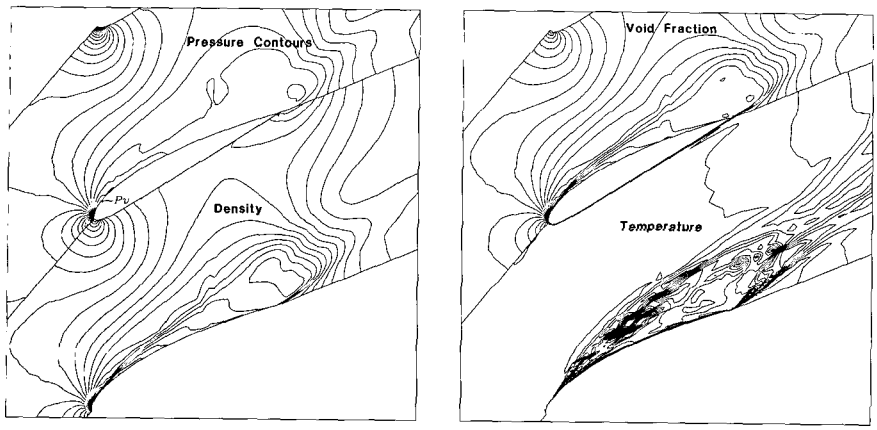

Fig.8 Time-averaged pressure, density, void fraction and temperature contours at σ=0.51

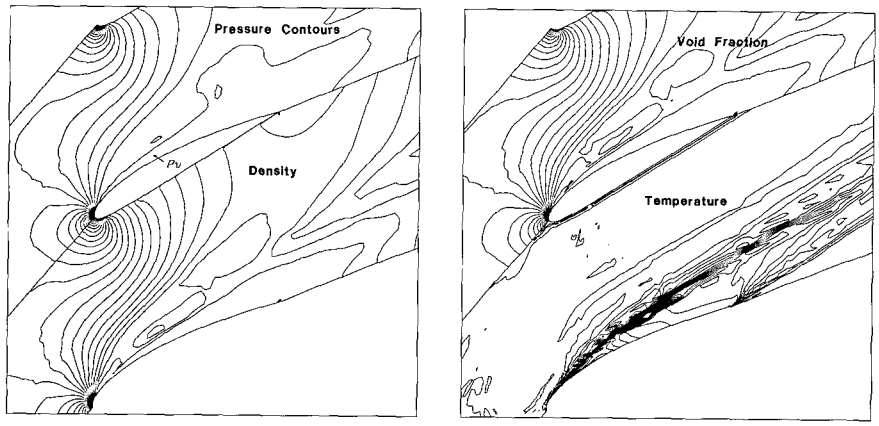

Fig.9 Time-averaged pressure, density, void fraction and temperature contours at σ=0.41

[12] Shin, B.R. and Ikohagi, T., Proc. 3rd Int. Symp. on Cavitation, Vol.2 (1998), p.301
[13] Yee, H.C., NASA TM-89469 (1987)
[14] van Leer, B., J. Comp. Phys., **32** (1979), p.101
[15] Shin, B.R. and Ikohagi, T., ASME FEDSM99-7215 (1999)
[16] Shin, B.R. et al., *Computational Fluid Dynamics 2000*, N. Satofuka (ed), Springer, Berlin (2001), p.651
[17] Iga, Y., Shin, B.R. and Ikohagi, T., Trans. JSME (2001), No. 01-0988
[18] Iga, Y., Shin, B.R. and Ikohagi, T., Trans. ASME (2001), Submitted.
[19] Chen, H.T. and Collins, R., J. Comp. Phys., **7** (1971), p.89
[20] Akagawa, K., *Gas-Liquid Two-Phase Flow*, Corona Pub. Tokyo (1974)
[21] Turkel, E., J. Comp. Phys., **72** (1987), p.277
[22] Choi, Y.H. and Merkle, C.L., J. Comp. Phys., **105** (1993), p.207
[23] Edwards, J.R. et al., AIAA J., **38** (2000), p.1624
[24] Clerc, S., J. Comp. Phys. **161** (2000), p.354
[25] Weiss, J.M. and Smith, W.A., AIAA J., **33** (1995), p.2050
[26] Beattie, D.R.H. and Whally, P.B., Int. J. Multiphase Flow, **8** (1982), p.83
[27] Roe, P.L., J. Comp. Phys., **43** (1981), p.357
[28] Murai, H. and Ibuki, S., Mem. Inst. High Speed Mech., Tohoku Univ., **47** (1981), p.117
[29] Shin, B.R. et al., JSME Int, J., **B-36** (1993), p.598
[30] Kikuchi, H., Mem. Inst. High Speed Mech., Tohoku Univ., **14** (1959), p.193
[31] Shin, B.R., 31st AIAA Fluid Dynamics Conference, AIAA 2001-2909 (2001)

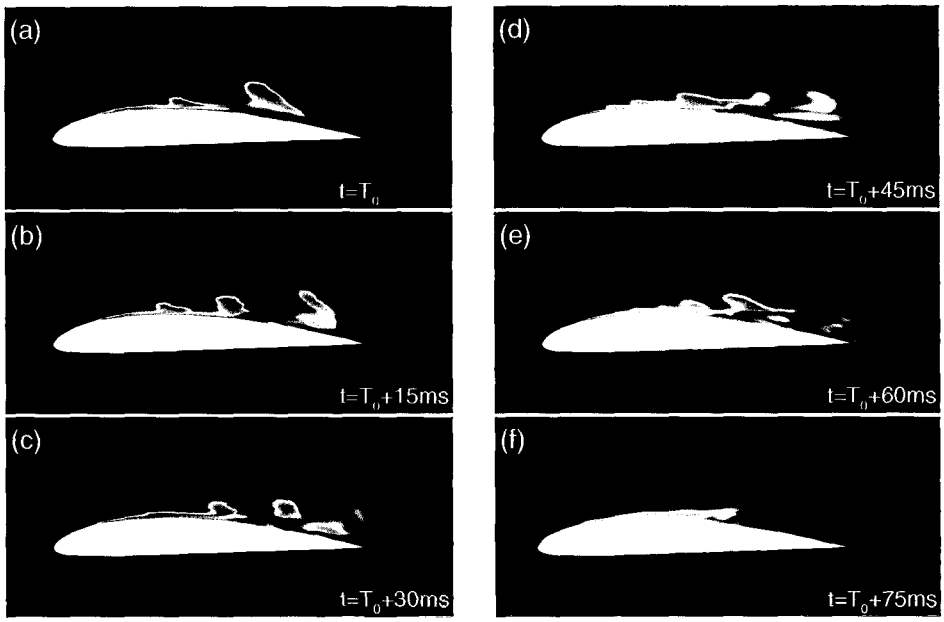

Fig.10 Time evolutions of void fraction at σ=0.6, $\alpha_i = 10.6°$ and Re=7×10^5

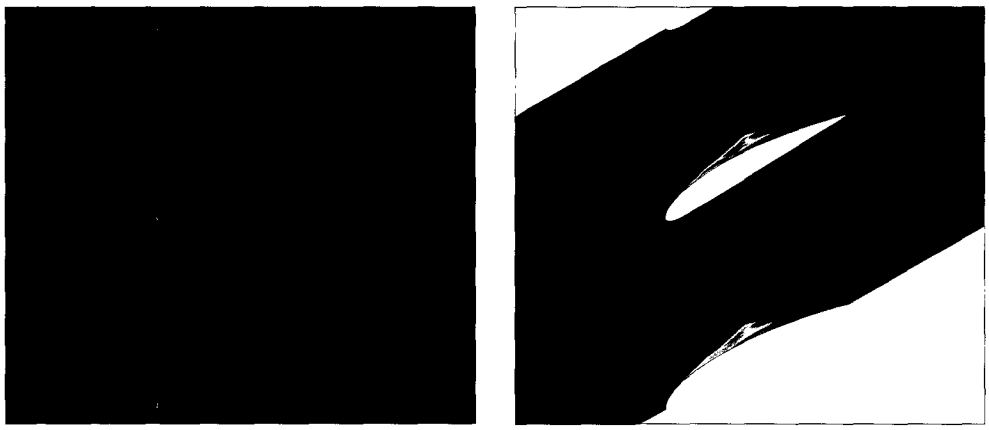

(a) Pressure (b) Void fraction

Fig.11 Time-averaged pressure and void fraction contours at σ=0.6 and $\alpha_i = 10.6°$